

Exploring the performance of superposition of product states: from 1D to 3D quantum spin systems

Apimuk Sornsang^{1,2} Itai Arad² and Dario Poletti^{1,2,3,4,*}

¹*Science, Mathematics and Technology Cluster, Singapore University of Technology and Design, 8 Somapah Road, 487372 Singapore*

²*Centre for Quantum Technologies, National University of Singapore 117543, Singapore*

³*Engineering Product Development Pillar, Singapore University of Technology and Design, 8 Somapah Road, 487372 Singapore*

⁴*MajuLab, CNRS-UNS-NUS-NTU International Joint Research Unit, UMI 3654, Singapore*

(Dated: 12th November 2025)

Tensor networks (TNs) are one of the best available tools to study many-body quantum systems. TNs are particularly suitable for one-dimensional local Hamiltonians, while their performance for generic geometries is mainly limited by two aspects: the limitation in expressive power and the approximate extraction of information. Here we investigate the performance of *superposition-of-product-states* (SPS) ansatz, a variational framework structurally related to canonical polyadic tensor decomposition. The ansatz does not compress information as effectively as tensor networks, but it has the advantages (i) of allowing accurate extraction of information, (ii) of being structurally independent of the geometry of the system, (iii) of being readily parallelizable, and (iv) of allowing analytical shortcuts. We first study the typical properties of the SPS ansatz for spin-1/2 systems, including its entanglement entropy, and its trainability. We then use this ansatz for ground state search in tilted Ising models—including one-dimensional and three-dimensional with short- and long-range interaction, and a random network—demonstrating that SPS can attain high accuracy.

I. INTRODUCTION

The primary difficulty in studying quantum many-body physics lies in the exponential growth of the Hilbert space as the number of particles increases [1, 2]. Various numerical and analytical tools have been developed to capture the ground state properties of quantum many-body systems. A prominent and very effective class of numerical methods is variational algorithms, which include, for example, variational Quantum Monte Carlo [3], Neural Quantum States [4, 5], and Tensor Network approaches [6–8]. Within the variational methods, we can list two main categories: those that sum over all the configurations, and those that use sampling. Variational Quantum Monte Carlo and Neural Quantum States belong to the latter category while tensor network algorithms typically belong to the first one. In tensor networks algorithms, full summation over all configurations (i.e., exact contraction of the network), is often infeasible, as it may require exponential computational cost. One is therefore led to using approximate tensor network contractions, such as Corner Transfer Matrix Renormalization Group (CTMRG) [8–10] boundary MPS [11, 12], and belief propagation to name a few [13–16]. However, in some of the most challenging simulations, even tensor network algorithms resort to sampling techniques [17–19].

When using these methods, errors can creep in for different reasons. For instance, when one performs samples, the expectation values may not be accurately estimated, leading to a sampling error. When using tensor networks

beyond one dimension, while one can sum over all configurations, the sum is evaluated in an approximated manner, which also can lead to errors.

In tensor networks, approximations stem either from reduced expressibility of the ansatz, or from the complexity of accurately extracting information from it. Here, we aim to use an ansatz which can readily be extended to multiple dimensions and from which one can readily and accurately extract information. Furthermore, the computations with this ansatz are highly parallelizable, leading to potential speed up.

From a physical point of view, the ansatz is a *Superposition of Product States* (SPS), which can be viewed as an extension of the bosonic Gutzwiller ansatz [20–22] to a superposition of non-orthogonal product states. From a more mathematical perspective, the SPS ansatz can be understood as a rank- M canonical polyadic (CP) decomposition of the tensor that is defined by coefficients of the underlying quantum state in the standard basis. This decomposition is also known as CANDECOMP/PARAFAC [23–25]. From this perspective, any tensor can be expressed as a sum of M rank-1 tensors, each formed by the tensor product of local vectors, with coefficients that weight the contribution of each rank-1 tensor. The expressive power of the SPS ansatz is controlled by the decomposition rank M , i.e., the number of product states in the decomposition.

The structure of the rest of this paper is as follows. In Sec. II, we formally present the construction of the SPS ansatz and examine its statistical properties, including typicality, expressive power, and trainability. In Sec. III, we benchmark the performance of the SPS ansatz in ground-state search tasks for various lattice geometries of the tilted Ising model, including 1D, 3D, long-range systems, and random coupling networks. A summary

* dario_poletti@sutd.edu.sg

and discussion of our findings are given in Sec. IV. For completeness, analytical derivations of the key quantities employed in our analysis are provided in App. A. We also provide details of the connectivity in the random-coupling system in App. B.

II. SPS ANSATZ

A superposition-of-product-states (SPS) ansatz for an L -sites quantum system is constructed by linearly combining M *normalized* product states with arbitrary amplitudes c_m . In general, this can be written as

$$|\Psi\rangle = \frac{|\Psi_u\rangle}{\sqrt{\mathcal{Z}}} = \frac{1}{\sqrt{\mathcal{Z}}} \sum_{m=1}^M c_m \bigotimes_{l=1}^L |\Psi_l^m\rangle, \quad (1)$$

with the unnormalized superposition of product states $|\Psi_u\rangle$, and $|\Psi_l^m\rangle$ is a state defined on a single site l . Since each product state is in general non-orthogonal to others, we have added the normalization $\mathcal{Z} := \langle \Psi_u | \Psi_u \rangle$. Equation (1) describes a general SPS ansatz.

In the following, we will focus on spin-1/2 systems whose ground states can be represented with real coefficients in the computational basis. Thus, in this work, we can specifically consider the following SPS ansatz

$$|\Psi_l^m\rangle := |\theta_l^m\rangle = \begin{pmatrix} \cos \theta_l^m \\ \sin \theta_l^m \end{pmatrix}, \quad (2)$$

where all parameters $\Theta := \{c_m, \theta_l^m\}$ are real-valued, resulting in a total of $(L+1)M$ parameters.

In the following, we are going to analyze statistical properties of the initially prepared arbitrary SPS in Sec. II A, particularly its normalization factor \mathcal{Z} (Sec. II A 1), the local observables (Sec. II A 2), and entanglement (Sec. II A 3), and then we further study its trainability in Sec. II B.

A. Statistics of the SPS ansatz

To examine the statistical behavior of the SPS ansatz $|\Psi\rangle$, we will analyze the expectation value and variance of a local observable, and further explore the expressive power of the ansatz via the entanglement entropy that it can produce. In this section, we consider a random SPS with θ_l^m initialized uniformly in $\mathcal{D}_\theta = [-\pi/2, \pi/2]$ and c_m in $\mathcal{D}_c = [-1, 1]$, thus, the SPS parameters Θ are drawn from $\mathcal{D} = \mathcal{D}_c^M \times \mathcal{D}_\theta^{LM}$.

1. Statistics of the norm

To further understand the global structure of the SPS states in Hilbert space, we first examine its normalization factor \mathcal{Z} to find how stable the ensemble is under random

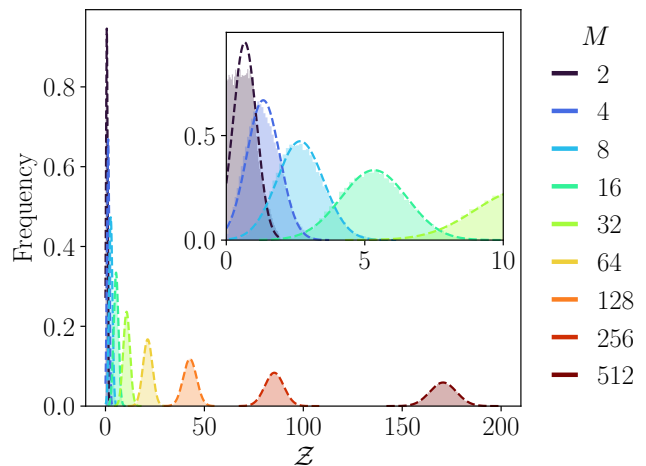


Figure 1. Distributions of 10,000 SPS norms \mathcal{Z} over \mathcal{D} for a system size $L = 20$ at different values of M . The norms are centered around $M/3$, with the spread increasing as M grows. The inset highlights the small- M regime, where clear deviations from the theoretical Gaussian form can be observed (dashed curves).

sampling. From Eqs. (1) and (2), we can analytically write the normalization constant as

$$\mathcal{Z} = \sum_{m,m'=1}^M c_m c_{m'} \prod_{l=1}^L \cos(\theta_l^m - \theta_l^{m'}).$$

Using well-known formulas describing the statistics of uniform distributions, we conclude that the diagonal terms, $m = m'$ contribute c_m^2 with $\mathbb{E}_{\mathcal{D}_c}[c_m^2] = 1/3$ and $\text{Var}_{\mathcal{D}_c}[c_m^2] = 4/45$. For off-diagonal terms, $m \neq m'$, the expectation value is vanishing due to the symmetry, while the variance scales exponentially as $1/(9 \cdot 2^L)$ (computational details are shown in App. A 1.) Therefore, using the central limit theorem, we conclude that for large M , the norm \mathcal{Z} is drawn from

$$\mathcal{Z} \sim \mathcal{N}\left(\frac{M}{3}, \frac{4M}{45} + \frac{M(M-1)}{9 \cdot 2^L}\right). \quad (3)$$

In the large- L limit, the off-diagonal terms become negligible, with the leading behavior governed by the coefficients c_m . Furthermore, we observe that the relative fluctuation of the norm, $\text{Var}_{\mathcal{D}}[\mathcal{Z}]/\mathbb{E}_{\mathcal{D}}[\mathcal{Z}]^2$, also vanishes for large M .

Fig. 1 demonstrates the normalization factor's distribution from 10,000 random SPSs. For small M , the quantum state with only a few product states retains an atypical structure—the norms are correlated sums of a small number of product-state contributions, and their distribution deviates substantially from the theoretical Gaussian distributions derived in Eq. (3) (dashed Gaussian curves in Fig. 1). When M increases, the distribution converges to the expected Gaussian distribution.

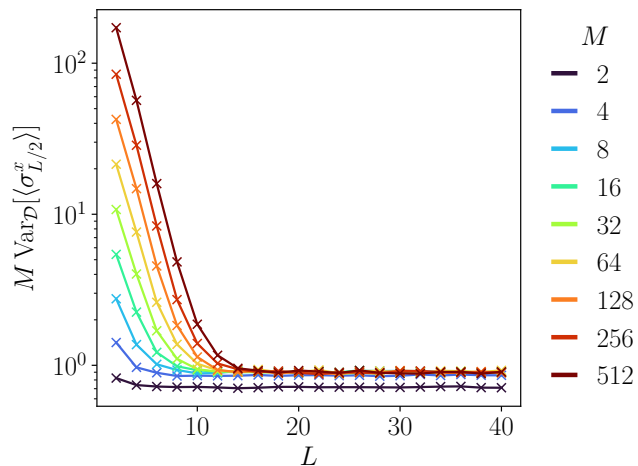


Figure 2. The variances of 10,000 values of $\langle \sigma_{L/2}^x \rangle$ over \mathcal{D} as a function of L for different M . The variances remain constant as L increases. This is an emergence of restricted typicality for the SPS ansatz in the large- M limit.

2. Statistics of local observables

We now consider the statistics of the expectation value of a single-site Pauli- X operator at site l , σ_l^x ,

$$\langle \sigma_l^x \rangle = \frac{1}{Z} \sum_{m,m'=1}^M c_m c_{m'} \sin(\theta_l^m + \theta_l^{m'}) \prod_{k \neq l} \cos(\theta_k^m - \theta_k^{m'}), \quad (4)$$

derived in App. A3. It is straightforward to verify that the expectation value $\langle \sigma_l^x \rangle$ vanishes on average, since $\mathbb{E}_{\mathcal{D}_\theta^2}[\sin(\theta_l^m + \theta_l^{m'})] = 0$ for all m and m' . In Fig. 2, we show that the variance of $\langle \sigma_l^x \rangle$ scales as $1/M$ with increasing M , and for sufficiently large L it becomes effectively independent of the system size. While the Haar-typical states display a much stronger concentration, with variances that decay exponentially in L [26], the SPS ansatz displays a complementary and robust form of *restricted typicality*, where fluctuations are suppressed polynomially in M , not suppressed exponentially.

Furthermore, the independence from L at large system sizes indicates that the observable retains consistent statistical behavior even in the thermodynamic limit. This stability also supports the ansatz's suitability for variational optimization, called *trainability*, where fluctuations of gradients do not vanish exponentially with L . We analyze in more detail the trainability in Sec. IIB.

3. Typical entanglement entropy

The evaluation of the entanglement entropy of the SPS ansatz serves as a key indicator of the *expressive power* of the ansatz. Entanglement reflects the degree of quantum correlation that can be represented between subsystems—higher typical entropy indic-

ates that the ansatz can capture more complex and correlated quantum states, whereas lower typical entropy suggests a more restricted expressive power confined to nearly separable configurations. To analyze the entanglement entropy, we evaluate the 2-Rényi entropy, $S_2(\rho_A) = -\ln \text{Tr}\{\rho_A^2\}$ of the reduced density matrix $\rho_A = \text{Tr}_B |\Psi\rangle\langle\Psi|$, where subsystem A corresponds to half of the all system. We focus on the 2-Rényi entropy since it is computationally more accessible than the von Neumann entropy while retaining the same qualitative behavior. Details for the computation of the 2-Rényi entropy within the framework of the SPS ansatz are shown in App. A2. Theoretically, the maximum of the 2-Rényi entropy is reached when the reduced density matrix becomes maximally mixed over the M product states, yielding $S_2^{\text{max}}(\rho_A) = \min\{\ln M, \frac{L}{2} \ln 2\}$ where $\frac{L}{2} \ln 2$ is the maximum entropy for a bipartite system.

Fig. 3(a) demonstrates that the typical 2-Rényi entropies, obtained from 10,000 random SPS realizations, become increasingly concentrated as M grows. However, Fig. 3(a) also reveals that the typical entropies remain below the theoretical maximum given by $\ln M$ and depicted by the dashed lines. Fig. 3(b) illustrates that the relative distance between the typical entropy and the maximum entropy does not vanish, but rather saturates for large L , even as M increases. In contrast to the SPS behaviour, a random MPS with local dimension equal to 2 and bond dimension χ obeys an area law with high probability. Ref. [27] and Theorem 4.7 of Ref. [28] show that the 2-Rényi entropy for a single bipartition of an open chain, the typical half-chain entropy satisfy $S_2 \approx \min\{\ln \chi, \frac{L}{2} \ln 2\} + O(\chi^{-1})$. This distinction highlights that while random MPS can reach the entanglement capacity allowed by their bond dimension, the SPS ansatz is inherently more restricted, which directly affects their expressive power and typical entanglement structure. This comparison confirms that the numerical analysis characterizes this limitation by revealing how the typical entanglement saturates below the theoretical bound.

B. Trainability

A main challenge in variational quantum algorithms is the *barren plateau* problem [29–32], where the gradient variance of loss functions decays exponentially with the system size [33], making optimization prohibitively difficult. This behavior typically emerges in highly entangled or randomly initialized ansätze, where the concentration of measure suppresses local gradient signals throughout the Hilbert space.

Since we are interested in searching for ground states, with a loss function corresponding to the energy of the system, we here examine the variance of the gradients of a local observable. Consider the ansatz in an L -site system; it is practical to focus on representative derivatives. We begin with the derivative of the site- $L/2$ expectation

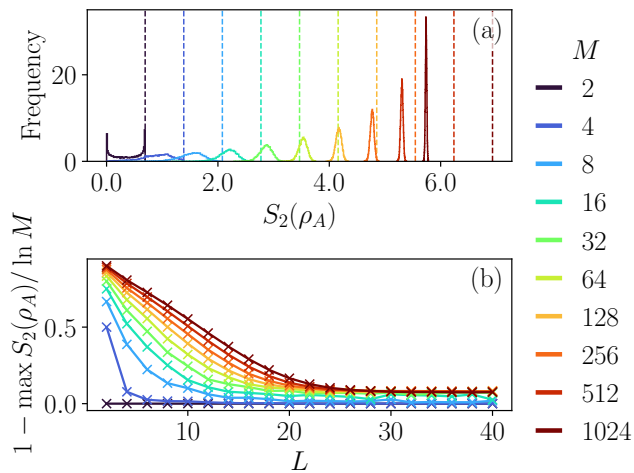


Figure 3. Typical 2-Rényi entropies obtained from 10,000 random SPS samples. (a) The distribution of the typical 2-Rényi entropies for $L = 20$. The entropies typically concentrate far from the theoretical maximum, even as M increases. (b) The minimum relative errors from the theoretical maximum saturate for larger L .

value $\langle \sigma_{L/2}^x \rangle$ with respect to the coefficients c_m , shown in Fig. 4(a) for $L = 20$ and $M = 32$ with 10,000 different realizations.

The variances of the gradients $\partial \langle \sigma_{10}^x \rangle / \partial c_m$ have not vanished across different m , indicating that these gradients remain essential across terms, thus shifting our focus towards θ_l^m . Next, we evaluate the derivatives with respect to θ_l^1 across all sites while considering only a term $m = 1$. As shown in Fig. 4(b), all gradients $\partial \langle \sigma_{10}^x \rangle / \partial \theta_l^1$ vanish except at the site directly coupled to the observable σ_{10}^x . This behavior indicates that although many subspaces appear flat and could resemble barren plateaus, the relevant local subspace associated with the observable retains finite gradients, thereby ensuring that optimization remains feasible in practice. We remark that, for the random nature of the SPS analyzed, the same results occur also when one considers local observables at other sites.

To gain more insight, we examine the variances of $\partial \langle \sigma_{L/2}^x \rangle / \partial c_1$ and $\partial \langle \sigma_{L/2}^x \rangle / \partial \theta_{L/2}^1$ as functions of the system size L for different M . Figs. 4(c,d) reveal that both variances scale as $1/M^2$ with increasing M , and eventually collapse on a single curve as L grows larger, even when M continues to increase. This scaling behavior highlights that the SPS ansatz retains trainability at large system sizes, in sharp contrast to the exponential decay characteristic of barren plateaus. This locality property further implies that the derivatives with respect to all θ_l^m remain non-vanishing for Hamiltonians composed of local observables. Hence, this observation provides strong evidence for the *absence* of a barren plateau in the SPS ansatz, making the ansatz *trainable*. Although this analysis does not directly assess task-specific

optimization, it only provides strong evidence that the SPS ansatz possesses favorable gradient landscapes that support efficient training in practice.

III. GROUND STATE SEARCH BY SPS ANSATZ

It has been established that the SPS ansatz is *trainable*, as its optimization does not suffer from barren plateaus. In this section, we present numerical results for the ground-state energies of tilted Ising models on various lattice geometries using the SPS ansatz. To identify the ground state within the SPS framework, we minimize the variational energy,

$$E_{\text{SPS}}(\Theta) = \langle \Psi | \mathcal{H} | \Psi \rangle, \quad (5)$$

by optimizing all variational parameters $\Theta = \{c_m, \theta_l^m\}$ where initially drawn from the uniform distributions in Sec. II A. Due to the product-state structure of the ansatz, the loss function can be expressed analytically as a function of trigonometric combinations of Θ (see App. A 3.) This analytic tractability can significantly speed up the optimization compared to fully black-box approaches (see Sec. III E.)

We focus on finding the ground-state energy of the tilted Ising model in the presence of a transverse field h_x and longitudinal field h_z , given by

$$\mathcal{H} = \sum_{(k,l)} J_{kl} \sigma_k^z \sigma_l^z - h_x \sum_{k=1}^L \sigma_k^x - h_z \sum_{k=1}^L \sigma_k^z, \quad (6)$$

where $\langle k, l \rangle$ denotes all connected pairs in an arbitrary lattice with L spins with coupling J_{kl} . We will consider nearest neighbour coupling in 1D and 3D configurations, 1D and 3D systems with power-law long-range interactions and a system with all-to-all coupling but such that only a random set of sites is coupled. To evaluate the quality of the ground state, we will plot the relative error from an accurate computation DMRG done with matrix product states—we will use the DMRG algorithm with a snake configuration of an MPS. To gain deeper insights into the performance of the SPS ansatz, we evaluate the ferromagnetic correlator

$$C_F = \frac{1}{L-1} \sum_{l \neq L/2}^L \langle \sigma_{L/2}^z \sigma_l^z \rangle - \langle \sigma_{L/2}^z \rangle \langle \sigma_l^z \rangle. \quad (7)$$

In this study, we focus exclusively on transitions between paramagnetic and ferromagnetic phases, by considering $J < 0$. This correlator has been computed using a DMRG ground state search algorithm. A ferromagnetic ground state is characterized by a large value of the ferromagnetic correlator C_F (indicated by the shaded purple region in Fig. 5), whereas a paramagnetic ground state driven by the transverse field yields a small correlator value (shaded orange). The portions of Fig. 5 with a white background are the region close to the phase transition boundary.

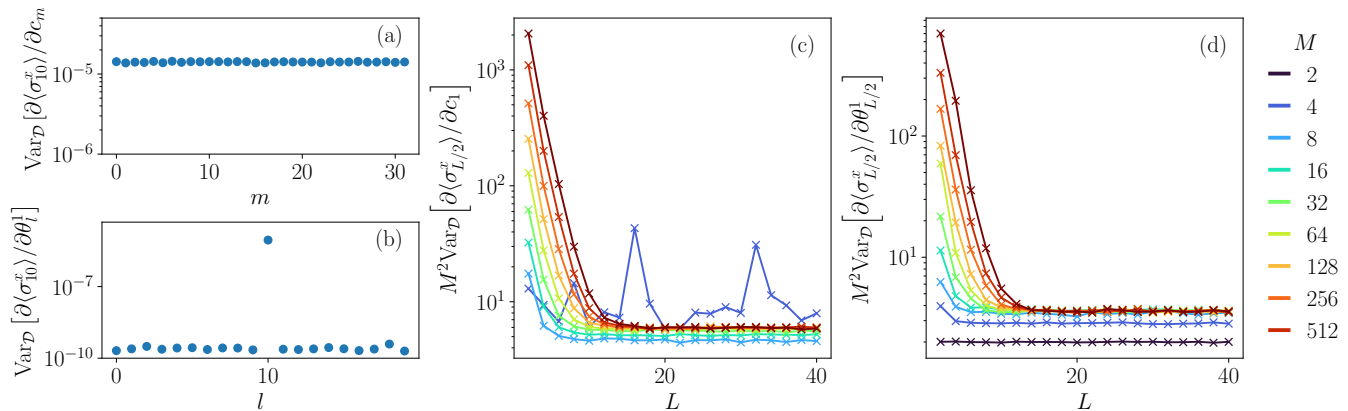


Figure 4. Trainability of the SPS ansatz is analyzed by evaluating the gradients of a local observable with respect to the variational parameters across 10,000 random samples. Panels (a) and (b) correspond to the case of $L = 20$ and $M = 32$. In panel (a), the gradients with respect to the coefficients c_m are identical across all m . In panel (b), fixing $m = 1$, the gradients with respect to the site index l vanish everywhere except at the site where the local observable is applied. Panels (c) and (d) display the gradient variances as functions of system size L and the number of product states M , focusing on derivatives with respect to c_1 and $\theta_{L/2}^1$, respectively. Although the case $M = 2$ in panel (c) shows fluctuations due to finite-sample effects, overall the variances decrease and saturate for large L , while decaying polynomially with M^2 . These results demonstrate that the SPS ansatz avoids barren plateaus, thereby ensuring efficient optimization even for large quantum systems.

A. Optimization

In our implementation, we employ the AdamW optimizer [34] with analytic gradients of the loss function $\partial E_{\text{SPS}}(\Theta)/\partial\Theta$ (see App. A 4) to iteratively refine the SPS parameters until convergence is achieved. We note, however, that when examining the coefficients $\{c_m\}$ in the paramagnetic regime, at times we might observe that several of them become negligibly small, which then results in the optimization being trapped in a local minimum. We counter this by implementing a *resampling* strategy. Specifically, in certain optimization steps, whenever any coefficients c_m fall below a predetermined threshold, we reinitialize both c_m and its corresponding set of angles $\{\theta_l^m\}_{l=1}^L$, drawn uniformly from the same distributions in Sec. II A. This approach helps to avoid wasting computational resources on product states that contribute little to the overall wavefunction, and it provides an opportunity to explore more promising regions of the parameter space.

In practice, the learning rate of the AdamW algorithm is 10^{-3} . The optimization epochs for each sample are 20,000 steps, and the resampling on the states with $c_m < 10^{-5}$ occurs every 5,000 epochs; thus, the resampling criteria happen 4 times in the optimization.

B. Implementation

In our implementation, the SPS ansatz is constructed and optimized within the PyTorch framework, which naturally supports GPU acceleration and parallelization, enabling efficient simulations of large system sizes. All SPS simulations are executed on nodes equipped with

NVIDIA A100 Tensor Core GPUs [35]. The benchmark ground-state energies are obtained using the DMRG algorithm, implemented in the TeNPy package [36], which is executed on CPUs AMD EPYC™ 7713 processors [35], where even for higher-dimensional lattices, the geometry is mapped into a one-dimensional snake-like configuration of MPS.

From the perspective of computational complexity, a single DMRG sweep over the chain scales as $O(L\chi^3)$ in time and $O(L\chi^2)$ in memory, where χ is the bond dimension of the MPS. Since practical convergence requires N_{sweep} full sweeps, the overall scaling is $O(N_{\text{sweep}}L\chi^3)$ in time. This makes DMRG highly efficient for systems with area-law entanglement but increasingly expensive for critical or higher-dimensional systems. By contrast, the SPS ansatz has a memory scaling as $O(LM)$, computes the expectation value and gradients of the Hamiltonian in $O(LM^2)$, and optimizes the SPS parameters in $O(LM^2T)$ where T is the number of optimization steps. The calculation details of the complexity are shown in Apps. A 3 and A 4.

C. Nearest-neighbor interactions

For 1D and 3D lattices with nearest-neighbor interactions and having open boundary conditions, we consider uniform coupling strengths defined by $J_{ij} = J$. In our experiments, we optimize the energy E_{SPS} with different $M = 1, 2, 4, \dots, 512$ for two models: a 40-qubits 1D ferromagnetic tilted Ising model with $J < 0$ and $h_z = 0.25|J|$ while varying $h_x/|J|$, and a $(4 \times 4 \times 4)$ -qubit 3D tilted Ising model on a cube lattice.

In practice, we first benchmark the SPS ansatz on a

Table I. Comparison between DMRG and SPS methods in terms of computational times for different systems. For DMRG, the bond dimension with the lowest energy E_{GS} is denoted by χ^* and χ for the bond dimension that the energy has a relative error ϵ_χ compared with E_{GS} . While for SPS, M represents the number of product states and ϵ the relative error compared with E_{GS} . The listed systems include 40-qubit one-dimensional (1D) and $(4 \times 4 \times 4)$ -qubit three-dimensional (3D) nearest-neighbor (NN) models, 40-qubit 1D and $(4 \times 4 \times 4)$ -qubit 3D long-range (LR) models with a specific $\alpha = 2.0$, and a 40-qubit random-coupling (RC) model with a specific $p = 0.4$. In this comparison, the system parameters are $(J, h_x, h_z) = (-1.0, 3.0, 0.25)$ for 1D and RC systems and $(-1.0, 7.0, 0.25)$ for 3D systems.

System	DMRG					SPS			
	χ^*	E_{GS}	χ	ϵ_χ	Time (s)	M	ϵ	CPU time (s)	GPU time (s)
1D NN	11	-3.10379965(1)	2	1.07×10^{-6}	8.21	512	1.00×10^{-3}	278.0 ± 9.6	7.08 ± 0.25
3D NN	512	-7.09401002(1)	8	1.89×10^{-3}	72.77	100	1.89×10^{-3}	27.47 ± 9.36	1.81 ± 0.44
1D LR	105	-3.16470959(4)	2	2.86×10^{-4}	13.06	256	1.00×10^{-3}	471.4 ± 139.0	7.37 ± 0.37
3D LR	128	-9.53603316(8)	4	3.71×10^{-5}	243.3	128	3.71×10^{-5}	140.7 ± 84.6	3.87 ± 1.77
RC	128	-8.65942219(1)	2	1.16×10^{-5}	17.24	32	1.16×10^{-5}	1.05 ± 0.74	0.65 ± 0.41

1D system by initializing 20 random instances and evaluating their performance. As shown in Fig. 5(a), the SPS ansatz can approximate the ground-state energy in the ferromagnetic phase with remarkable accuracy. The relative error, defined as

$$\epsilon := \frac{E_{SPS} - E_{GS}}{E_{GS}}, \quad (8)$$

is small also when compared against the ground-state energy E_{GS} obtained from the DMRG algorithm. For small h_x , a single product state ($M = 1$), the minimum relative error ϵ_{\min} can reach values as low as 10^{-8} . As the transverse field h_x increases, however, the accuracy depends more strongly on the number of product states M . Near the critical region, the performance with small M is significantly reduced, consistent with the required growth of the bond dimension in a DMRG algorithm at criticality.

In the paramagnetic phase, optimization with larger M yields moderate improvements, and while the achieved accuracy is lower than in the ferromagnetic regime, the relative errors remain fairly small, underscoring the robustness of the ansatz. Ref. [37] showed that translationally invariant MPSs can always be written either as a single product state or as a superposition of only a few such states. Since the paramagnetic ground state is effectively translationally invariant only in the bulk, the observed performance degradation can be attributed primarily to boundary effects.

We further test the SPS ansatz on a 3D system. The results, shown in Fig. 5(b), demonstrate that the SPS ansatz maintains good performance in the low- h_x regime, but its accuracy deteriorates more noticeably as the transverse field strength increases, particularly in the vicinity of the phase transition ($h_x \approx 2.8$). This behavior highlights both the expressive power and the limitations of the SPS ansatz—it efficiently captures ground states in the ferromagnetic regions, but requires larger M to remain accurate in the critical region or for the paramagnetic regions.

D. Long-range and random interactions

To further investigate the performance of the SPS ansatz in ground-state searches, we carry out additional numerical experiments on tilted Ising models with long-range and randomly coupled interactions. For the long-range interaction, we will consider an experimentally relevant one (e.g. in trapped ions) that can be modeled using a power-law decay: $J_{kl} = J/d(k, l)^\alpha$, where J sets the interaction strength, $d(k, l)$ is an Euclidean distance between site k and l on a lattice where each nearest-neighbor pair has a unit length proximity, and α determines the spatial decay of correlations. For the random coupling system, a pair of sites is connected with probability p and interacted with uniform strength J . The model parameters are fixed to $J < 0$, $h_x = 3.0|J|$, and $h_z = 0.25|J|$ for 1D and random coupling systems, and $h_x = 7.0|J|$ with the same J and h_z for a 3D system, corresponding to the paramagnetic regime in the short-range limit (large α in long-range system). In these experiments, we systematically vary both the interaction-range exponent α and the coupling probability p , respectively. Note that we use DMRG algorithms to obtain the ground-state energies in practice and use the snake configuration for a 3D system.

Figs. 5(c,d) show the minimum relative error ϵ_{\min} for each interaction range exponent α , evaluated over 20 different random initializations on 40-qubit 1D and $(4 \times 4 \times 4)$ -qubit 3D long-range systems, respectively. When $\alpha = 0$, corresponding to a fully connected interaction, the SPS ansatz achieves low relative errors, with ϵ_{\min} reaching the order of 10^{-8} . As α increases—resulting in shorter-range interactions—the minimum relative error ϵ_{\min} also becomes larger. This trend mirrors changes in the system’s ferromagnetic correlator C_F (7), which is illustrated as the background color in Figs. 5(c,d). Similar to the nearest-neighbor case, we observe that lower ferromagnetic correlations are associated with higher relative errors.

For the 40-qubit tilted Ising model defined on a random-connecting graph, where interactions are disordered and each edge is present with probabilities $p \in$

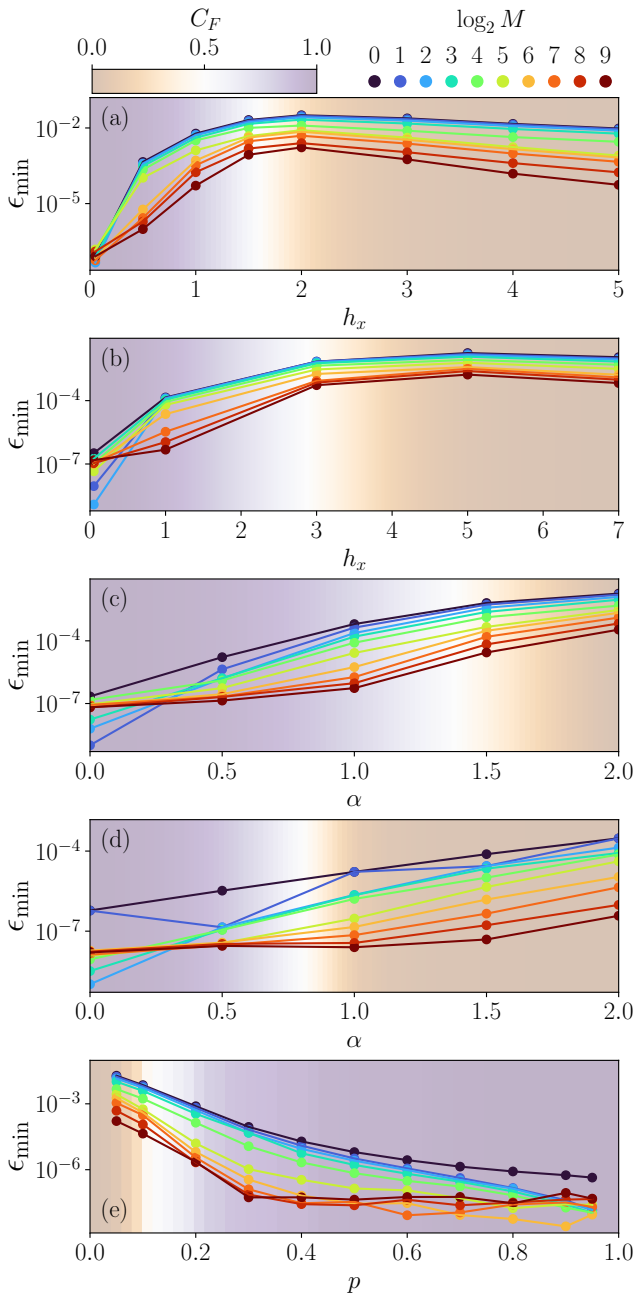


Figure 5. The performances in the ground state searches with the SPS ansatz. The performances with different $M \in \{1, 2, 4, \dots, 512\}$ are quantified by the minimum relative error, from 20 different initialized SPS parameters, in the SPS ansatz’s approximation of the ground state energy compared to the target ground state energy E_{GS} for a tilted Ising model with $J = -1$, $h_z = 0.25$ on (a) 40-qubit 1D nearest-neighbor connection for $h_x \in \{0.05, 0.5, 1.0, 1.5, 2.0, 3.0, 4.0, 5.0\}$, (b) $(4 \times 4 \times 4)$ -qubit 3D nearest-neighbor connection for $h_x = \{0.05, 1.0, 3.0, 5.0, 7.0\}$, (c) 40-qubit 1D all-to-all connection for $\alpha \in \{0.0, 0.5, 1.0, 1.5, 2.0\}$ with $(J, h_x, h_z) = (-1, 3.0, 0.25)$, (d) $(4 \times 4 \times 4)$ -qubit 3D all-to-all connection for $\alpha \in \{0.0, 0.5, 1.0, 1.5, 2.0\}$ with $(J, h_x, h_z) = (-1, 7.0, 0.25)$, and (e) 40-qubit random connected graph for $p \in \{0.05, 0.1, 0.2, 0.3, 0.4, 0.5, 0.6, 0.7, 0.8, 0.9, 0.95\}$. The gradient background is shaded according to the ferromagnetic correlator C_F , with lighter shading corresponding to lower values.

$\{0.05, 0.1, 0.2, 0.3, 0.4, 0.5, 0.6, 0.7, 0.8, 0.9, 0.95\}$, the SPS ansatz continues to perform effectively. In practice, we use the same random seed in every random graph generation, and the adjacency matrices are given in App. B. As shown in Fig. 5(e), even in this highly irregular interaction landscape, relative errors as small as 10^{-5} are achieved with around $M \sim 100$ product states. This result highlights the robustness of the SPS framework—despite the absence of translational symmetry and the presence of disorder, the ansatz can still capture the essential features of the ground state with moderate resources. In particular, the ability to handle disordered systems suggests that the SPS ansatz may be a flexible variational tool beyond clean, uniform models.

For $\alpha = 0$ in long-range systems, and large p , e.g., $p \geq 0.6$, in random coupling, the systems become (almost) uniformly all-to-all interaction, yielding a ground state close to a low-entanglement state. Accordingly, a small M in the SPS ansatz already captures the essential structure, while a larger M primarily increases the parameter space and hinders optimization under a fixed compute budget. As a result, within the same training time, large M can exhibit higher relative errors than small M , reflecting the optimization effect rather than limited expressivity.

E. Comparison

To have a quantitative benchmark of the SPS ansatz, we compare its ability to reach the ground-state energy with that of the DMRG algorithm under the same relative-error target (when obtainable within a manageable value of M , i.e. beyond 1D). We focus on the paramagnetic regime for which the SPS ansatz generally requires larger values of M , compared to small values for χ in the DMRG code. The ground-truth energies, E_{GS} , are obtained from DMRG at a bond dimension χ^* chosen such that the energy change between consecutive doublings of the bond dimension ($\chi = 2, 4, 8, \dots$) is below 10^{-10} ; see Table I.

We consider system sizes matching those in the previous section and use the following parameters: $(J, h_x, h_z) = (-1, 3.0, 0.25)$ for 1D and random-coupling systems, and $(J, h_x, h_z) = (-1, 7.0, 0.25)$ for 3D systems. For long-range interactions we set $\alpha = 2.0$, and for random-coupling systems we use $p = 0.4$. The SPS ansatz is optimized with AdamW (learning rate $\eta = 0.1$) and training stops once the SPS energy E_{SPS} reaches the prescribed relative-error threshold. The SPS runtimes reported in Table I are means \pm standard deviations over 40 realizations where the initial SPS parameters are drawn from the distribution described in Sec. II A.

To ensure a fair comparison, we benchmark DMRG and SPS on identical hardware: first on a CPU-only node with an AMD EPYC™ 7713 processor. We additionally show the computational time on a GPU node equipped with an NVIDIA A100 [35]. In 3D and random-coupling

systems, the SPS ansatz typically reaches the target relative error faster than DMRG, with further speedups observed on the GPU. In contrast, for 1D systems DMRG remains highly efficient with short runtimes, whereas the SPS ansatz often does not attain the same relative-error threshold, reflecting the optimality of DMRG for 1D systems.

IV. CONCLUSIONS

The SPS ansatz provides a compact variational framework built from a superposition of product states, directly linked to a rank- M CP decomposition of a quantum state tensor, making the ansatz efficient, scalable, and highly parallelizable. We found that the ansatz exhibits restricted typicality, where local observables are partially stable across random instances, but their variances display polynomial decreases on M instead of exponential scaling. Regarding the expressive power, we have shown that for a random SPS, the 2-Rényi entropy of the reduced density matrix exhibits an amount of entanglement comparable to the maximum expressible by the ansatz. A central strength of the SPS ansatz is its trainability, whereby analysis of the variance of the gradients confirm the absence of barren plateaus. Local observables retain non-vanishing gradients, and their variances decay polynomially with M and saturate with L , guaranteeing efficient optimization even in large systems. Despite its

simplicity, we have shown that the SPS ansatz is expressive enough to approximate nontrivial quantum correlations and achieves strong performance in ground-state searches. It captures ordered and paramagnetic phases with high accuracy, and remains effective in disordered settings such as long-range and random-coupling tilted Ising models.

The limited performance of the SPS ansatz in the paramagnetic phase suggests that incorporating spatial modulation in the ansatz could be a natural and promising extension. By allowing site-dependent structure in the variational parameters, the ansatz can capture weak correlations beyond mean-field descriptions, thereby broadening its expressive power in more strongly correlated regimes. Future works would also focus on extending the ansatz to complex-valued quantum states, for the evaluation of more complex ground states, and for the description of time-evolving systems.

ACKNOWLEDGMENT

D.P. and A.S. acknowledges the support of the Ministry of Education, Singapore, under the grant T2EP50123-0017, and from HTX under project HTX000ECI24000267. D. P. acknowledges fruitful discussions with D. Rossini and G. Vignale. The computational work was performed at the National Supercomputing Centre, Singapore [35].

-
- [1] L. D. Landau and E. M. Lifshitz, *Quantum Mechanics II: Advanced Topics* (Elsevier, 2015) chapter on Many-Body Systems.
 - [2] M. A. Nielsen and I. L. Chuang, *Quantum Computation and Quantum Information* (Cambridge University Press, 2010).
 - [3] W. M. Foulkes, L. Mitas, R. Needs, and G. Rajagopal, Quantum monte carlo simulations of solids, *Reviews of Modern Physics* **73**, 33 (2001).
 - [4] G. Carleo and M. Troyer, Solving the quantum many-body problem with artificial neural networks, *Science* **355**, 602 (2017).
 - [5] D. Wu, R. Rossi, F. Vicentini, N. Astrakhantsev, *et al.*, Variational benchmarks for quantum many-body problems, *Science* **386**, 296 (2024).
 - [6] U. Schollwöck, The density-matrix renormalization group in the age of matrix product states, *Annals of Physics* **326**, 96 (2011).
 - [7] R. Orús, A practical introduction to tensor networks: Matrix product states and projected entangled pair states, *Annals of physics* **349**, 117 (2014).
 - [8] F. Verstraete and J. I. Cirac, Renormalization algorithms for quantum-many body systems in two and higher dimensions, *arXiv preprint cond-mat/0407066* (2004).
 - [9] T. Nishino and K. Okunishi, Corner transfer matrix renormalization group method, *Journal of the Physical Society of Japan* **65**, 891 (1996).
 - [10] R. Orús and G. Vidal, Simulation of two-dimensional quantum systems on an infinite lattice revisited: Corner transfer matrix for tensor contraction, *Physical Review B* **80**, 094403 (2009).
 - [11] J. Jordan, R. Orús, G. Vidal, F. Verstraete, and J. I. Cirac, Classical simulation of infinite-size quantum lattice systems in two spatial dimensions, *Physical review letters* **101**, 250602 (2008).
 - [12] M. Weyrauch and M. V. Rakov, Efficient mps algorithm for periodic boundary conditions and applications, *arXiv preprint arXiv:1303.1333* (2013).
 - [13] E. Robeva and A. Seigal, Duality of graphical models and tensor networks, *Information and Inference: A Journal of the IMA* **8**, 273 (2019).
 - [14] R. Alkabetz and I. Arad, Tensor networks contraction and the belief propagation algorithm, *Physical Review Research* **3**, 023073 (2021).
 - [15] S. Sahu and B. Swingle, Efficient tensor network simulation of quantum many-body physics on sparse graphs, *arXiv preprint arXiv:2206.04701* (2022).
 - [16] C. Guo, D. Poletti, and I. Arad, Block belief propagation algorithm for two-dimensional tensor networks, *Physical Review B* **108**, 125111 (2023).
 - [17] A. W. Sandvik and G. Vidal, Variational quantum monte carlo simulations with tensor-network states, *Physical review letters* **99**, 220602 (2007).
 - [18] L. Wang, I. Pizorn, and F. Verstraete, Monte carlo simulation with tensor network states, *Physical Review B* **83**,

- 134421 (2011).
- [19] A. J. Ferris and G. Vidal, Perfect sampling with unitary tensor networks, *Physical Review B* **85**, 165146 (2012).
- [20] D. S. Rokhsar and B. G. Kotliar, Gutzwiller projection for bosons, *Phys. Rev. B* **44**, 10328 (1991).
- [21] W. Krauth, M. Caffarel, and J.-P. Bouchaud, Gutzwiller wave function for a model of strongly interacting bosons, *Phys. Rev. B* **45**, 3137 (1992).
- [22] D. Jaksch, C. Bruder, J. I. Cirac, C. W. Gardiner, and P. Zoller, Cold bosonic atoms in optical lattices, *Phys. Rev. Lett.* **81**, 3108 (1998).
- [23] F. L. Hitchcock, The expression of a tensor or a polyadic as a sum of products, *Journal of Mathematics and Physics* **6**, 164 (1927).
- [24] J. D. Carroll and J.-J. Chang, Analysis of individual differences in multidimensional scaling via an n-way generalization of "eckart-young" decomposition, *Psychometrika* **35**, 283 (1970).
- [25] R. A. Harshman, Foundations of the parafac procedure: Models and conditions for an "explanatory" multi-modal factor analysis, *UCLA working papers in phonetics* **16**, 84 (1970).
- [26] P. Facchi, S. Pascazio, and F. V. Pepe, Quantum typicality and initial conditions, *Physica Scripta* **90**, 074057 (2015).
- [27] B. Collins, C. E. González-Guillén, and D. Pérez-García, Matrix product states, random matrix theory and the principle of maximum entropy, *Communications in Mathematical Physics* **320**, 663 (2013).
- [28] J. Haferkamp, C. Bertoni, I. Roth, and J. Eisert, Emergent statistical mechanics from properties of disordered random matrix product states, *PRX Quantum* **2**, 040308 (2021).
- [29] J. R. McClean, S. Boixo, V. N. Smelyanskiy, R. Babbush, and H. Neven, Barren plateaus in quantum neural network training landscapes, *Nature communications* **9**, 4812 (2018).
- [30] M. Cerezo, A. Arrasmith, R. Babbush, S. C. Benjamin, S. Endo, K. Fujii, J. R. McClean, K. Mitarai, X. Yuan, L. Cincio, *et al.*, Variational quantum algorithms, *Nature Reviews Physics* **3**, 625 (2021).
- [31] M. Larocca, S. Thanasilp, S. Wang, K. Sharma, J. Biamonte, P. J. Coles, L. Cincio, J. R. McClean, Z. Holmes, and M. Cerezo, Barren plateaus in variational quantum computing, *Nature Reviews Physics* , 1 (2025).
- [32] K. Srimahajariyapong, S. Thanasilp, and T. Chotibut, Connecting phases of matter to the flatness of the loss landscape in analog variational quantum algorithms, *arXiv preprint arXiv:2506.13865* (2025).
- [33] T. Barthel and Q. Miao, Absence of barren plateaus and scaling of gradients in the energy optimization of isometric tensor network states, *Communications in Mathematical Physics* **406**, 86 (2025).
- [34] I. Loshchilov and F. Hutter, Decoupled weight decay regularization, *arXiv preprint arXiv:1711.05101* (2017).
- [35] <http://nsccl.org>.
- [36] J. Hauschild, J. Unfried, S. Anand, B. Andrews, M. Bintz, U. Borla, S. Divic, M. Drescher, J. Geiger, M. Hefel, K. Hémerly, W. Kadow, J. Kemp, N. Kirchner, V. S. Liu, G. Möller, D. Parker, M. Rader, A. Roman, S. Scalet, L. Schoonderwoerd, M. Schulz, T. Soejima, P. Thoma, Y. Wu, P. Zechmann, L. Zweng, R. S. K. Mong, M. P. Zaletel, and F. Pollmann, Tensor network Python (TeNPy) version 1, *SciPost Phys. Codebases* , 41 (2024).
- [37] M. Florido-Llinàs, Á. M. Alhambra, R. Trivedi, N. Schuch, D. Pérez-García, and J. I. Cirac, The product structure of mps-under-permutations, *arXiv preprint arXiv:2410.19541* (2024).

Appendix A: Analytical formulations

A notable advantage of the SPS ansatz is its analytic tractability. In contrast to many variational families that require heavy numerical sampling, several physical quantities can be computed explicitly. Now, we present the analytic formulas for the mean and the variance of the norm \mathcal{Z} , for the 2-Rényi entropy, for local observables within the SPS framework, and for the gradients of the local observables with respect to the SPS parameters.

1. Mean and variance of an SPS norm

Starting from the SPS norm \mathcal{Z} , each parameter is independent, allowing us to compute the expectation values of individual terms separately. For the diagonal term, since the probability density function of c_m is uniform with $p(c_m) = 1/2$, the expectation value of c_m^2 is

$$\mathbb{E}_{\mathcal{D}_c}[c_m^2] = \frac{1}{2} \int_{-1}^1 c_m^2 dc_m = \frac{1}{3}. \quad (\text{A1})$$

Similarly, the variance of c_m^2 is

$$\begin{aligned} \text{Var}_{\mathcal{D}_c}[c_m^2] &= \frac{1}{2} \int_{-1}^1 c_m^4 dc_m - (\mathbb{E}_{\mathcal{D}_c}[c_m^2])^2 \\ &= \frac{4}{45}. \end{aligned} \quad (\text{A2})$$

Since there are M diagonal terms, their total variance contribution is $4M/45$.

For the off-diagonal terms, the expectation value vanishes due to the symmetry of the cosine function. Given that the probability density of each θ_l^m is $p(\theta_l^m) = 1/\pi$, we have

$$\begin{aligned} \text{Var}_{\mathcal{D}_\theta^2} \left[\cos(\theta_l^m - \theta_l^{m'}) \right] &= \frac{1}{\pi^2} \int_{-\frac{\pi}{2}}^{\frac{\pi}{2}} \int_{-\frac{\pi}{2}}^{\frac{\pi}{2}} \cos^2(\theta_l^m - \theta_l^{m'}) d\theta_l^m d\theta_l^{m'} \\ &= \frac{1}{2}, \end{aligned} \quad (\text{A3})$$

and $\text{Var}_{\mathcal{D}_c^2}[c_m c_{m'}] = 1/9$. Since each off-diagonal term of \mathcal{Z} involves L multiplicative factors and $M(M-1)$ summations, the total variance contribution becomes $M(M-1)/(9 \cdot 2^L)$. Thus, the overall variance of the SPS norm can be written as

$$\text{Var}_{\mathcal{D}}[\mathcal{Z}] = \frac{4M}{45} + \frac{M(M-1)}{9 \cdot 2^L}. \quad (\text{A4})$$

2. 2-Rényi entropy

Considering the reduced density matrix ρ_A of a bipartition of the system, within the SPS ansatz framework, we can simply write the reduced density matrix as

$$\rho_A = \frac{1}{\mathcal{Z}} \sum_{m,m'=1}^M c_m c_{m'} \bigotimes_{l=1}^{L/2} |\theta_l^m\rangle \langle \theta_l^{m'}| C_B^{mm'}, \quad (\text{A5})$$

where $C_B^{mm'} = \prod_{l=L/2+1}^L \langle \theta_l^m | \theta_l^{m'} \rangle$ and $\langle \theta_l^m | \theta_l^{m'} \rangle = \cos(\theta_l^m - \theta_l^{m'})$. Then the trace of the square of the reduced density matrix can also be written in the same way,

$$\text{Tr} \rho_A^2 = \frac{1}{\mathcal{Z}^2} \sum_{m,m',n,n'=1}^M c_m c_{m'} c_n c_{n'} C_B^{mm'} C_A^{m'n} C_B^{nn'} C_A^{n'm} \quad (\text{A6})$$

where $C_A^{mm'} = \prod_{l=1}^{L/2} \langle \theta_l^m | \theta_l^{m'} \rangle$. In practice, we can implement this quantity using

$$\text{Tr} \rho_A^2 = \frac{1}{\mathcal{Z}^2} \text{Tr}(\mathcal{C}_B \mathcal{C}_A \mathcal{C}_B \mathcal{C}_A) \quad (\text{A7})$$

where $\mathcal{C}_A = (C_A^{mn})_{mn}$ and $\mathcal{C}_B = (c_m c_n C_B^{mn})_{mn}$. From Eq. (A7), we can thus readily evaluate the 2-Rényi entropy, which is simply written as $S_2(\rho_A) = -\ln \text{Tr} \{\rho_A^2\}$.

In the complexity analysis, building each contraction matrix \mathcal{C} requires $O(LM^2)$ operations and $O(M^2)$ memory. The final evaluation of Eq. (A7) then scales as $O(M^2(L+M))$ with the same memory usage, where the $O(M^3)$ term originates from the dense matrix multiplications.

3. Local Observables

In the analyses of typicality, trainability, and ground-state search with the SPS ansatz, the computation relies on expectation values of local observables. This section introduces the analytic formulations of these local observables.

Considering, for instance, the Pauli- X operator at site k , σ_k^x , the expectation value is given by

$$\langle \sigma_k^x \rangle = \frac{1}{\mathcal{Z}} \langle \Psi_u | \sigma_k^x | \Psi_u \rangle.$$

At the site k , the matrix element takes the form

$$\begin{aligned} \langle \theta_k^m | \sigma_k^x | \theta_k^{m'} \rangle &= (\cos \theta_k^m \quad \sin \theta_k^m) \begin{pmatrix} 0 & 1 \\ 1 & 0 \end{pmatrix} \begin{pmatrix} \cos \theta_k^{m'} \\ \sin \theta_k^{m'} \end{pmatrix} \\ &= \cos \theta_k^m \sin \theta_k^{m'} + \sin \theta_k^m \cos \theta_k^{m'} \\ &= \sin(\theta_k^m + \theta_k^{m'}) \end{aligned}$$

and otherwise are the overlap terms $\langle \theta_l^m | \theta_l^{m'} \rangle = \cos(\theta_l^m - \theta_l^{m'})$. Defining $C^{mm'} = \prod_{l=1}^L \langle \theta_l^m | \theta_l^{m'} \rangle$, the expectation value can be written compactly as

$$\langle \sigma_k^x \rangle = \frac{\sum_{m,m'=1}^M c_m c_{m'} C^{mm'} X_k^{mm'}}{\sum_{m,m'=1}^M c_m c_{m'} C^{mm'}} \quad (\text{A8})$$

where

$$X_k^{mm'} = \frac{\sin(\theta_k^m + \theta_k^{m'})}{\cos(\theta_k^m - \theta_k^{m'})},$$

called the *Pauli-X tensor*, which is the same form shown in Eq. (4). This formulation enables us to compute local expectation values with a time complexity of $O(LM^2)$.

For σ_k^z operator, the corresponding local term is

$$\begin{aligned} \langle \theta_k^m | \sigma_k^z | \theta_k^{m'} \rangle &= (\cos \theta_k^m \quad \sin \theta_k^m) \begin{pmatrix} 1 & 0 \\ 0 & -1 \end{pmatrix} \begin{pmatrix} \cos \theta_k^{m'} \\ \sin \theta_k^{m'} \end{pmatrix} \\ &= \cos \theta_k^m \cos \theta_k^{m'} - \sin \theta_k^m \sin \theta_k^{m'} \\ &= \cos(\theta_k^m + \theta_k^{m'}). \end{aligned}$$

Thus, in Eq. (A8), the term $X_k^{mm'}$ is replaced by

$$Z_k^{mm'} = \frac{\cos(\theta_k^m + \theta_k^{m'})}{\cos(\theta_k^m - \theta_k^{m'})},$$

called the *Pauli-Z tensor*, as expressed in detail in

$$\langle \sigma_k^z \rangle = \frac{\sum_{m,m'=1}^M c_m c_{m'} C^{mm'} Z_k^{mm'}}{\sum_{m,m'=1}^M c_m c_{m'} C^{mm'}}. \quad (\text{A9})$$

This can be readily extended to multi-body operator. For instance, for the two-body interaction $\sigma_k^z \sigma_{k+1}^z$, the contributions to the expectation value factorize into $Z_k^{mm'} Z_{k+1}^{mm'}$.

These compact analytic forms make the evaluation of local observables highly efficient, scaling only polynomially with M and L , which requires $O(LM^2)$ operations with $O(M^2)$ resources.

4. Gradients of the expectation value

The SPS ansatz allows for an analytical evaluation of the derivative of the expectation value of a local observable with respect to any ansatz parameter in Θ , as utilized in Secs. II B and III. In particular, the derivative of

the energy with respect to an SPS parameter ϑ is given by

$$\frac{\partial E_{\text{SPS}}}{\partial \vartheta} = \frac{1}{\mathcal{Z}} \frac{\partial \langle \Psi_u | \mathcal{H} | \Psi_u \rangle}{\partial \vartheta} - E_{\text{SPS}} \frac{1}{\mathcal{Z}} \frac{\partial \mathcal{Z}}{\partial \vartheta}. \quad (\text{A10})$$

Since the unnormalized expectation value of the Hamiltonian, $\langle \mathcal{H} \rangle_u := \langle \Psi_u | \mathcal{H} | \Psi_u \rangle$, is composed of unnormalized local Pauli expectation values, the derivative with respect to θ_l^m depends only on the site index l and is independent of m . As an example, for the derivative of the unnormalized local observable $\langle \sigma_k^x \rangle_u$ with respect to c_m , we have

$$\begin{aligned} \frac{\partial \langle \sigma_k^x \rangle_u}{\partial c_m} &= 2 \sum_{m'=1}^M c_{m'} \sin(\theta_k^m + \theta_k^{m'}) \prod_{l \neq k}^L \cos(\theta_l^m - \theta_l^{m'}) \\ &= 2 \sum_{m'=1}^M c_{m'} C^{mm'} X_k^{mm'}, \end{aligned} \quad (\text{A11})$$

where the factor of 2 arises from the symmetry between the indices m and m' .

For the derivative with respect to θ_l^m , two cases can be distinguished: (i) for $l = k$ and (ii) for $l \neq k$.

(i) For $l = k$, the derivative is

$$\begin{aligned} \frac{\partial \langle \sigma_k^x \rangle_u}{\partial \theta_k^m} &= 2 \sum_{m'=1}^M c_m c_{m'} \cos(\theta_k^m + \theta_k^{m'}) \prod_{l \neq k}^L \cos(\theta_l^m - \theta_l^{m'}) \\ &= 2 \sum_{m'=1}^M c_m c_{m'} C^{mm'} Z_k^{mm'}. \end{aligned} \quad (\text{A12})$$

This expression maintains the same structural form as the Pauli- Z tensor $Z_k^{mm'}$, which can be directly reused from the computation of the energy term E_{SPS} .

(ii) For $l \neq k$, the derivative becomes

$$\begin{aligned} \frac{\partial \langle \sigma_k^x \rangle_u}{\partial \theta_l^m} &= -2 \sum_{m'=1}^M c_m c_{m'} \sin(\theta_k^m + \theta_k^{m'}) \\ &\quad \prod_{p \neq l, k}^L \cos(\theta_p^m - \theta_p^{m'}) \sin(\theta_l^m - \theta_l^{m'}) \\ &= -2 \sum_{m'=1}^M c_m c_{m'} C^{mm'} X_k^{mm'} \frac{\sin(\theta_l^m - \theta_l^{m'})}{\cos(\theta_l^m - \theta_l^{m'})} \\ &= -2 \sum_{m'=1}^M c_m c_{m'} C^{mm'} X_k^{mm'} \tan(\theta_l^m - \theta_l^{m'}), \end{aligned} \quad (\text{A13})$$

which adds the extra tangent function beside the Pauli- X tensor.

Similarly, for the local Pauli- Z operator, we have

$$\frac{\partial \langle \sigma_k^z \rangle_u}{\partial \theta_k^m} = -2 \sum_{m'=1}^M c_m c_{m'} C^{mm'} X_k^{mm'} \quad (\text{A14})$$

and

$$\frac{\partial \langle \sigma_k^z \rangle_u}{\partial \theta_l^m} = -2 \sum_{m'=1}^M c_m c_{m'} C^{mm'} Z_k^{mm'} \tan(\theta_l^m - \theta_l^{m'}) \quad (\text{A15})$$

for $l \neq k$. In general, for two-body terms, taking the derivative with respect to a parameter associated with one operator site transforms the corresponding Pauli tensor into another tensor of the same family.

Finally, the derivative of the normalization factor \mathcal{Z} is

$$\frac{\partial \mathcal{Z}}{\partial \vartheta} = \begin{cases} 2 \sum_{m'=1}^M c_{m'} C^{mm'} : \vartheta = c_m, \\ -2 \sum_{m'=1}^M c_m c_{m'} C^{mm'} \tan(\theta_l^m - \theta_l^{m'}) : \vartheta = \theta_l^m. \end{cases} \quad (\text{A16})$$

As shown above, the gradient expressions with respect to the SPS parameters Θ can be implemented analytically, eliminating the need for automatic differentiation and enabling efficient parallel benchmarking during computation.

Appendix B: Connectivity in random coupling system

This section describes the connectivity structure of a random-coupling lattice generated with varying connection probability p . In the implementation, a random number generator from the NumPy package is used with a fixed seed (set to 5) to ensure reproducibility. Each possible pair of nodes (i, j) , with $i < j$, is connected independently with probability p . The resulting graph is generally equivalent to an Erdős-Rényi $G(L, p)$ network. The adjacency matrices for the different values of the probability of having connected links p are pictorially given in Fig. 6.

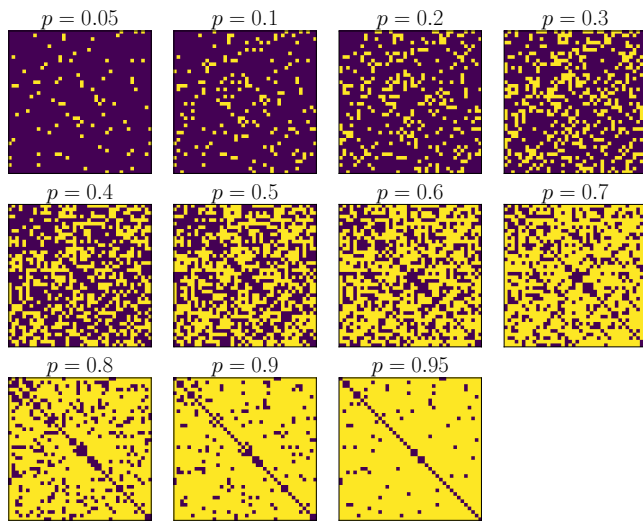


Figure 6. Adjacency matrices of randomly connected graphs in various connection probability p . Purple and yellow denote matrix elements with values 0 and 1, respectively.